PAPER

Check for updates

Stoichiometrically optimized e_g orbital occupancy of Ni–Co oxide catalysts for Li–air batteries†

Shadeepa Karunarathne, [iD] [a] Yasun Y. Kannangara, [iD] [b] Chirag R. Ratwani, [iD] [a] Chanaka Sandaruwan, [iD] [b] W. P. S. L. Wijesinghe, [iD] [b] Ali Reza Kamali [iD] [c,d] and Amr M. Abdelkader [iD] *[a]

Li–air battery (LAB) technology is making continuous progress toward its theoretical capacity, which is comparable to gasoline. However, the sluggish reaction at the cathode is still a challenge. We propose a simple strategy to optimize the surface e_g occupancy by adjusting the stoichiometric ratios of transition metal-based spinel structures through a controlled hydrothermal synthesis. Three distinct stoichiometries of Ni–Co oxides were used to demonstrate the direct correlation between stoichiometry and catalytic performance. The groundsel flower-like structure having a 1 : 1.4 Ni : Co atomic ratio with high surface area, high defect density, and an abundance of Ni^{3+} at the surface with semi-filled e_g orbitals was found to benefit the structure promoting high catalytic activities in aqueous and aprotic media. The assembled LAB cells employing this cathode demonstrate an exceptional lifespan, operating for 3460 hours and completing 173 cycles while achieving the highest discharge capacity of 13 759 mA h g^{-1} and low charging overpotentials. The key to this prolonged performance lies in the full reversibility of the cell, attributed to its excellent OER performance. A well-surface adsorbed, amorphous LiO_2/Li_2O_2 discharge product is found to possess high diffusivity and ease of decomposition, contributing significantly to the enhanced longevity of the cell.

Introduction

High-density renewable energy storage is becoming increasingly important due to the limited availability of fossil fuels and the global demand for renewable energy sources.[1,2] Metal–air battery technology is a promising sustainable green energy storage alternative, which consists of a metallic anode (*e.g.*, Li, K, Na, Zn, Fe, and Al), a porous cathode, and a compatible electrolyte.[3] Aprotic Li–air batteries (LABs) are considered the best possible alternative since they offer the highest possible theoretical energy density (11.4 kW h kg^{-1}) and specific capacity (1170 A h kg^{-1}).[4] A successful LAB is yet to be commercialized owing to the sluggish air cathode reaction kinetics and related parasitic reactions associated with oxygen reduction reaction (ORR) and oxygen evolution reaction (OER)

occurring during the discharging and charging steps, respectively.[5] These sluggish kinetics and parasitic reactions lead to fast decay in battery performance through an accumulation of undecomposed discharged products at the cathode surface.[6,7]

A better-performing bifunctional catalyst should help the LAB sustain a large number of cycles with low overpotential and high efficiency by promoting oxygen kinetics and controlling the discharged product morphology.[8] In recent years, enormous efforts have been made to develop suitable bifunctional catalysts that could be incorporated into the cathode architecture. Noble metals remain at the top of the list of high-performing catalysts.[9,10] However, excessive costs limit the practical usage of noble metals and their derivatives in LABs.[11] Numerous low-cost alternatives have shown promising results, such as doped/undoped carbon[12] and derivatives of non-precious transition metals, including their oxides,[13] and sulfides.[14] Despite their decent ORR activity owing to their suitable pore structure and high conductivity, carbonaceous materials were found to be susceptible to reduced oxygen compounds (ROC) and singlet oxygen ($^1O_2$) generated during the charging cycle, and Gallant *et al.* observed that the whole carbon cathode surface oxidizes forming insulating Li_2CO_3 as it reacts with Li_2O_2 present in the proximity of the surface.[15] Since potentials over 3.82 V are needed to decompose Li_2CO_3, higher charging overpotentials are needed during the OER,

[a] Faculty of Science and Technology, Bournemouth University, Talbot Campus, Poole, BH12 5BB, UK. E-mail: aabdelkader@bournemouth.ac.uk

[b] Sri Lanka Institute of Nanotechnology, Pitipana, Homagama, Sri Lanka

[c] Energy and Environmental Materials Research Centre (E^2MC), Northeastern University, Shenyang, 110819, China. E-mail: ali@mail.neu.edu.cn

[d] Department of Materials Science and Metallurgy, University of Cambridge, Cambridge, UK. E-mail: a.r.kamali@cantab.net

leading to further cell decomposition as it is exposed to more active ROS and singlet oxygen.[16] The search is currently ongoing to find alternative stable cathode materials. Transition metal oxides (TMOs) have demonstrated encouraging performances in the past few years, specifically due to their high stability during OER,[17] motivating further research in the field.[18] Among the many TMOs explored, binary spinel structures like $CoFe_2O_4$,[18] and $NiFe_2O_4$[19] produced decent bifunctional activity for Li–air batteries, where the mixed valences in AB_2O_4 spinel structures contribute to enhancing the catalytic activity and obtaining good electrical conductivity, overcoming the inherent insulating nature of TMOs.[20] In particular, $NiCo_2O_4$ has gained considerable attention due to its excellent electrochemical properties.[21]

Nevertheless, the high intrinsic resistivity and the limited catalytic activity of TMOs limit their performances as long-lasting stable catalysts, and using carbon-rich highly resistive binders further amplifies the instability as commonly used binders such as PVDF, PAN, PVC, and PVP were found to be unstable to Li_2O_2,[22] and hence, binder-free cathodes were preferred.[23] Further, recently it was identified that the catalytic activity in transition metal-based catalysts could be enhanced by tuning the e_g orbital occupation, where a low occupancy in the e_g orbitals with a higher number of unsaturated coordination cations is found to lead to the formation of strong bonds between reaction intermediates, improving the oxygen reaction kinetics. Different orbital engineering and facet engineering techniques such as alloying,[24] doping,[25] selective facet growth,[26] and forming heterostructures[27] were found to be successful so far in altering the orbital occupancy in transition metal-based catalysts used in LABs.

Important parameters that have yet to receive adequate attention in the existing literature pertain to the impact of the spinel binary oxide stoichiometry, the effects of associated stoichiometric defects on the electronic properties of the catalyst, and the effects of the stoichiometry on the electrode's electrochemical performance. In this research, we explore this gap by producing three distinct Ni–Co oxide stoichiometries with dissimilar morphological features, achieved through precise control of nucleation and crystal growth under hydrothermal conditions. Amongst the tested structures, interestingly, the defect-rich inverted spinel structure, formed into a hierarchical groundsel flower-like microstructure directly anchored on the fur-like surface grown on the Ni foam, yielded the best catalytic activity. This structure, having a 1.38 Ni : Co stoichiometry and high Ni^{3+}/Ni^{2+} and Co^{2+}/Co^{3+} ratios, with plentiful unsaturated coordination cations, exhibited exceptional OER and ORR performances in both aqueous and aprotic media, with only 1.56 V needed to reach 10 mA cm^{-2} current density and a halfwave potential of 0.89 V in the respective OER and ORR studies in the aqueous medium. Additionally, it displayed excellent Li–air battery performance, boasting a specific discharge capacity of 13 759 mA h g^{-1} and a remarkable cyclability of 173 cycles, further demonstrating the key attributes of the synthesized porous binary oxide 3D network with favourable e_g orbital occupation, stoichiometry, and facets supporting fast oxygen

redox kinetics and large depositions of the discharged products. Further analysis of the discharged and recharged electrodes found that the high diffusivity and the easy decomposability of the formed amorphous discharge product helped the efficient and durable cyclability of the battery, while the resistance shown by the binder-free binary oxide cathode against the parasitic reaction involving ROC and singlet oxygen helped the sustainable operation with full recovery. These findings highlight the importance of the study, providing deeper insight into optimizing the stoichiometry of binary oxides to obtain favourable e_g orbital occupation for enhanced Li–air battery operation.

Experimental section

Synthesis of *in situ* electrocatalyst-loaded electrodes

The $NiCo_2O_4$ electrocatalysts were directly grown on the surface of a Ni foam using a hydrothermal method. In a typical synthesis, 2.5 mmol of $Ni(NO_3)_2 \cdot 6H_2O$, 5 mmol of $Co(NO_3)_2 \cdot 6H_2O$, and 10 mmol of urea were dissolved in 100 ml of deionized water, and 70 ml of the solution was transferred into a 100 ml Teflon-lined stainless steel autoclave vessel. The surface of the Ni foam was prepared suitable for catalyst growth by degreasing the surface *via* ultrasonic cleaning in an ethanol/DI (deionized) water mixture, followed by etching out the surface oxide layer using diluted HCl and HNO_3 acid solutions. A 5×2 cm piece of well-cleaned, freshly prepared Ni foam was vertically immersed in the precursor-filled autoclave vessel, and the vessel was heated at 5 °C min^{-1} before being maintained at 120 °C for 12 h. After letting the autoclave vessel cool down to room temperature, the catalyst-coated Ni foams were collected and washed thoroughly with DI water before air drying at 60 °C for 12 hours. The dried samples were calcined for 4 hours at 400 °C with a ramping rate of 5 °C min^{-1} in the air to obtain the final product, NCO 120, which was found to be loaded with catalyst material at ~0.8 mg cm^{-2}. For comparison, two other catalysts were synthesized under different thermodynamic environments by maintaining the autoclave at 150 °C (NCO 150) and 180 °C (NCO 180) for 12 hours, respectively, as shown in Fig. S1†, while keeping the other parameters the same.

Materials characterization

The crystalline phases of the synthesized materials were identified using X-ray powder diffraction (XRD) on a Siemens D5000 diffractometer with Cu K_α radiation (Siemens, Germany). The morphology of the synthesized $NiCo_2O_4$ catalysts was examined using scanning electron microscopy (SEM, HITACHI SU6600), and the microstructure and crystallinity of the samples were further examined using transition electron microscopy (TEM, JEOL JEM-2100) combined with selected area electron diffraction (SAED) and inverse-fast Fourier transform (FFT). The Brunauer–Emmett–Teller (BET) surface area was measured using N_2 adsorption/desorption at 77.3 K on an Autosorb iQ Station 1 after the samples were degassed at

150 °C for 12 h under vacuum before physisorption measurements. X-ray photoelectron spectroscopy (XPS) was performed using an ESCALB 250Xi spectrophotometer (Thermo Fisher, USA). Al kα radiation was used with a spot size of 900 μm and monitored beam values of 14.4 kV (anode HT) and 18.08 mA (beam current). All XPS measurements were performed in constant analyzer energy (CAE) mode with a 2000 eV ion energy and with the mid-range current used for 30 seconds to clean the surface.

Electrochemical measurements

The OER and ORR performances of the as-prepared *in situ* coated electrocatalysts were evaluated using a three-electrode setup attached to an IviumStat system, where the catalyst grafted Ni foam was used as the working electrode while Pt foil and saturated calomel electrodes were used as counter and reference electrodes, respectively. 1 M KOH was used as the electrolyte, and all the measured potentials were transformed to the RHE following the formula $E_{(RHE)} = E_{(SCE)} + 0.241 + 0.059 \times pH$. The working electrodes were activated through cyclic voltammetry (CV) tests at 100 mV s^{-1} before CV and linear sweep voltammetry (LSV) measurements. The OER LSV measurements were carried out at a rate of 10 mV s^{-1} under a saturated Ar atmosphere, while ORR LSV polarisation curves were recorded at a scan rate of 5 mV s^{-1} with rotation rates ranging from 0 to 1500 rpm in a saturated O$_2$ environment. Electrochemical impedance spectroscopy (EIS) was performed for the frequency range of 1 MHz to 0.01 Hz with a 5 mV sinusoidal signal. Further, the catalyst's long-term stability was studied with chronopotentiometric measurements with a current density of 10 mA cm^{-2}.

The Li–air battery CR-2032 type meshed coin cells were assembled in an Ar-filled glovebox, where 13 mm disks of 0.5–0.8 mg cm^{-2} catalyst loaded Ni foam were used as the battery cathode while 1 mm thick Li foil, Celgard 2500 membrane, and 1 M LiTFSI in tetraethylene glycol dimethyl ether (TEGDME) solution were used as the anode, separator, and the electrolyte, respectively. Assembled batteries were kept in a sealed dry air environment at 1 atm for 5 h before electrochemical analysis. CV analysis of the Li–air cells was conducted in the 2.0–4.5 V *vs.* Li/Li$^+$ potential window at 0.5 mV s^{-1} using an IviumStat system, and galvanostatic discharge/charge analysis was performed using a Neware battery analyzer where the specific capacities and current densities were calculated considering the amount of active material present in the battery cathode. EIS, SEM, and Raman microscopy techniques were utilized for discharge product analysis.

Results and discussion

Material characterization

The Ni–Co oxide catalyst nanostructures were *in situ* grafted on Ni foam using a hydrothermal technique. The synthesis technique is known to produce non-stoichiometric hydroxide structures with crystal imperfections[28] mostly in terms of substitu-

tional disorder (atoms in a given site are replaced by another atom) leading to the occurrence of point defects or extended defects in the calcined binary oxide nano-crystalline structure. Hence, the process helped to optimize the stoichiometry of the derived Ni–Co oxide spinel structure, forming a favourable electronic structure for faster oxygen kinetics.

Scanning electron microscopy (SEM) images identified the differently synthesized NCOs' distinct morphological and structural features. Fig. 1(a)–(d) indicate that the NCO 120 structure has a well-interconnected groundsel flower-like 3D morphology directly anchored on the Ni foam, and the remaining surface of the Ni foam is well covered with fur-like grown NiCo$_2$O$_4$ as depicted in Fig. 1(d). Further, SEM images of NCO 120 in Fig. 1(b and c) and the histogram presented in Fig. S2† verify the hierarchical growth nature of catalyst microstructures on the Ni foam with a narrow particle size distribution (5.28 ± 1.19 μm) in addition to the identified petal diameter of ∼30 nm (see Fig. 1(c)). This hierarchical structure can provide a high surface area to exploit many exposed active sites and simultaneously leave enough voids for improved O$_2$/air diffusion. Fig. 1(c) further indicates that the given reaction parameters promote the unidirectional growth of the crystal to form the final groundsel flower-like structure by assembling many needle-like nanostructures. As the hydrothermal reaction temperature is increased to 150 °C, it is observed that the structure of the material (NCO 150) is further opened to form a chrysanthemum flower-like morphology, as indicated in Fig. 1(e), where the crystal growth seems to expand towards the second direction while keeping the well-interconnected architecture (see Fig. S3†). The SEM images in Fig. 1(f) and Fig. S4† suggest further expansion of the structure as the reaction temperature is increased to 180 °C by exfoliation of individual petals into a lamellar-like 2D morphology, where bidirectional crystal growth is well exhibited. The modification of the morphology closely follows the dissolution–precipitation mechanism related to nucleation and crystal growth in hydrothermal synthesis.[29] The increase in crystal size, accompanied by a more open architectural structure (leading to a 2D morphology), can be attributed to the higher convection and diffusion rates resulting from the elevated reaction temperatures and ramping rates in both NCO 150 and NCO 180. These different temperature regimes induce granular growth in different directions, allowing shifts in crystal facets and stoichiometries. EDS elemental mapping (refer to Fig. 1, panels g–j) confirms the uniform presence of Ni, Co, and O within the synthesized NCO 120 structure, whereas the fur-like coating and particles exhibit a comparatively lower concentration of Ni than the Ni foam.

XRD patterns of various as-synthesized NCO structures were analyzed to identify their characteristic crystalline phases. The NCO powder was first detached from the Ni substrate to prevent any overlap with the diffraction signals from the substrate, as previously reported.[30] The XRD pattern in Fig. 2(a) shows that the synthesized materials have a similar nano-crystalline cubic spinel structure. The diffraction peaks present at 2θ = 19.0°, 31.1°, 36.8°, 44.7°, 55.5°, 59.1°, and 65.1° could be
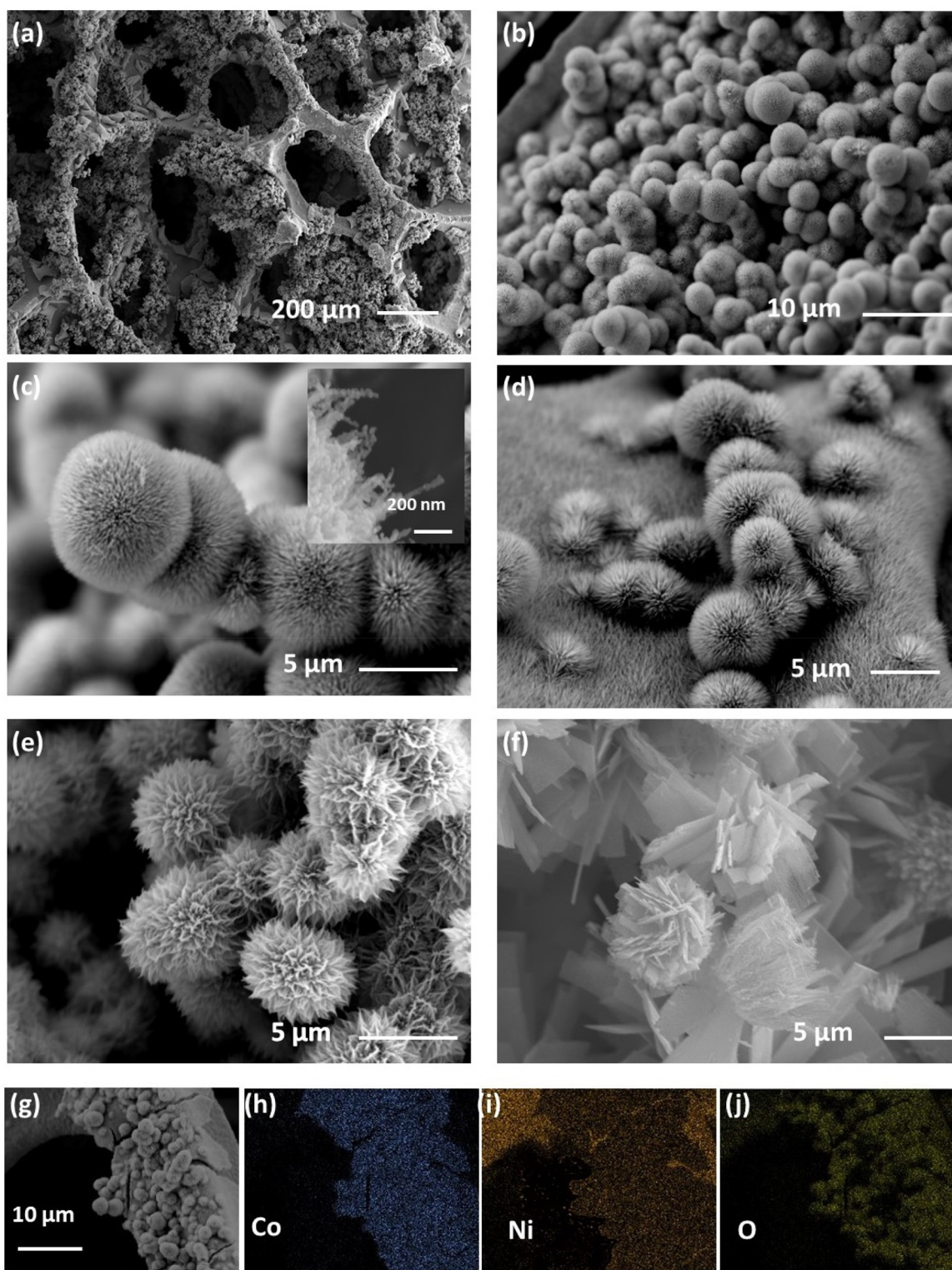
Fig. 1 SEM images of different Ni–Co oxide structures anchored on Ni foam, (a–d) low and high magnifications of the NCO 120 structure, (e) NCO 150, (f) NCO 180, and (g–j) EDX analysis of the NCO 120 structure.

assigned to the (111), (220), (311), (422), (400), (511), and (440) planes respectively, mostly in agreement with the typical XRD pattern for spinel cubic $NiCo_2O_4$ (JCPDS no. 20-0781, $a = b = c$ = 8.11 Å), consistent with the previous reports.[31] The other small diffraction peak present in the spectrum around 43.8° is due to the presence of residual Ni from the Ni foam. It is
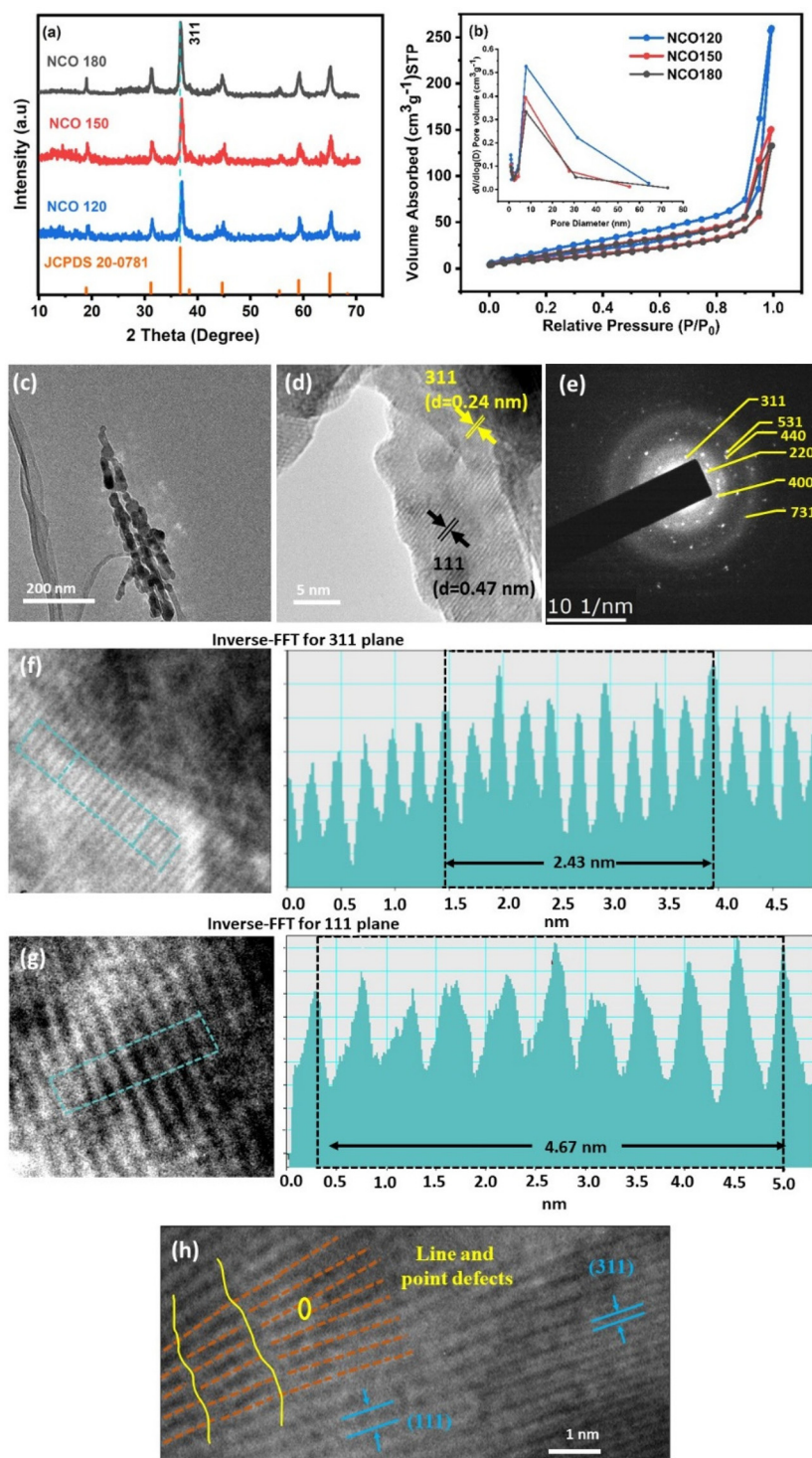
Fig. 2   (a) XRD patterns of the synthesized $NiCo_2O_4$ structures on Ni foam, (b) nitrogen adsorption/desorption isotherms and pore size distribution curve of $NiCo_2O_4$ structures, (c) TEM image, (d) HRTEM image, (e) corresponding SAED pattern, (f and g) inverse-FFT analysis for the NCO 120 structure, and (h) crystal defects.

worth noting that the XRD spectrum is more diffused for NCO 120, and much sharper diffraction peaks can be observed for NCO 180. Further, a small mismatch in the 311 peak, more distinctly with the NCO 120 structure, can be observed, and this could be due to an offset in the Ni : Co stoichiometry. The shift of the diffraction peak towards the higher angles with lower temperatures could suggest the formation of more Ni-rich compounds, possibly by replacing Co^{2+} ions with Ni^{3+}

ions with a smaller ionic radius. Such a phenomenon aligns with the concept of the partial inversion of spinel crystal structures, where peak shifts and the decrease in intensity are related to a low crystallinity material with increased disorder[32] as the tetrahedral Co^{2+} sites exchanged with octahedral Ni^{3+}, reducing the symmetry of the structure.[33]

TEM, HR-TEM, SAED, and inverse-FFT were used to further study the microstructures of the NCO samples, including their morphological and crystalline lattice properties. The TEM image of an individual petal of the NCO 120 microstructure (Fig. 2(c)) shows that the petals are assemblies of small crystals of size varying from 25–40 nm in diameter. The selected-area electron diffraction (SAED) pattern with well-defined diffraction spots in Fig. 2(e) reveals the presence of crystalline Ni–Co oxides. The diffraction spots aligned well with the planes indexed during the XRD studies. The high-resolution TEM image of the same structure showed the lattice fringes with d-spacings at about 0.24 nm and 0.47 nm, corresponding to the 311 and 111 crystallographic planes of $NiCo_2O_4$, respectively (Fig. 2(d)). As indicated in the inverse-FFT analysis presented in Fig. 2(f and g), the calculated interplanar distances of 0.243 nm and 0.467 nm for the respective 311 and 111 planes are marginally lower than the reported d-spacings in JCPDS no. 20-0781, in agreement with the observed peak shift in the XRD analysis. The dominant surface planes of 111 and 311 are rare for $NiCo_2O_4$, providing indirect evidence of stoichiometric shifts, where the surface is known to be dominated by the 220 plane along with the 111 plane in most cases (including NCO 150 presented in Fig. S5†) for $NiCo_2O_4$.[34] More importantly, the image in Fig. 2(h) identifies the frequent presence of point defects (or extended defects) on the crystal facets. The defects could arise by substitution of Co^{2+} ions at octahedral sites of the spinel structure with Ni^{3+} ions. In such a scenario, since the substituted Ni^{3+} ion at the octahedral site prefers to have tetrahedral coordination, the surrounding oxygen anion matrix can get distorted, and extended defects could arise by missing one or two out of the six oxygen anion coordinates. These observations were in line with the XRD results discussed previously and will be further discussed along with the XPS studies.

The characteristic N_2 adsorption–desorption isotherm curves obtained at 77.3 K for the three NCO materials are presented in Fig. 2(b). All of the materials present type IV isotherm H3 hysteresis behaviour with calculated BET surface areas of 62.31, 45.21, and 39.02 $m^2\ g^{-1}$ for NCO 120, NCO 150, and NCO 180, respectively. Further, the NCO 120 catalyst contains a large number of mesopores with pore diameters ranging from ~5–30 nm and a large pore volume of 54.11 $cm^3\ g^{-1}$. This mesoporous structure with higher pore volume is reported to support high discharge capacity by accommodating a large quantity of the discharged products. Also, the mesoporous structure with a higher surface area promotes full reversibility of LAB cells with lower interfacial resistance by keeping the discharged products well attached and within the structure of the cathode surface.[35]

Surface chemical states and the composition of the three different synthesized Ni–Co oxide catalyst materials were studied using XPS analysis. The survey scan in Fig. 3(a) and S6† confirmed the presence of Ni, Co, and O in all three synthesized structures. As indicated in Fig. 3(b), Co 2p spectra of all three samples can be deconvoluted into well-fitted two spin–orbit doublets and shakeup satellites, where the peaks fitted at 779.7 and 794.5 eV correspond to Co^{3+} valence, while the peaks at 780.9 and 795.9 eV are assigned to Co^{2+}.[36] Similarly, the high-resolution Ni 2p spectra in Fig. 3(d) can also be fitted with two spin–orbit doublets and shakeup satellites. The peaks at 853.7 and 871.1 eV are assigned to Ni^{2+}. The peaks at 855.9 and 873.0 eV can be assigned to Ni^{3+} valence.[37] The peaks positioned at 529.5, 531.1, and 532.6 eV in the O 1s spectra in Fig. 3(c) typically correspond to metal-bonded oxygen, defect sites with low oxygen coordination, and surface adsorbed hydroxyl groups in water molecules, respectively.[38]

As indicated in Fig. 3(e), NCO 120 possesses the highest amount of oxygen vacancies, corresponding to 38% of the total envelope. Further, XPS results provide evidence confirming that defects could arise by the substitution of Co^{2+} ions at octahedral sites of the spinel structure by Ni^{3+} ions, where high Ni^{3+}/Ni^{2+} and Co^{2+}/Co^{3+} ratios can be observed in the NCO 120 structure. As mentioned, the preference for tetrahedral coordination of the substituted Ni^{3+} ions at octahedral sites, distorting the surrounding oxygen anion matrix by missing one or two out of the six oxygen anion coordinates, is understood to be the mechanism of the formation of the vacancy sites. These differences in the metallic ion ratios in the derived spinel structure were achieved by altering the reaction conditions during the hydrothermal synthesis. The NCO 180 catalyst with the least substitutions and closer stoichiometry (1.74) to the standard 2.0 Co/Ni stoichiometry for the $NiCo_2O_4$ structure was synthesized at a relatively higher temperature of 180 °C with more favourable thermodynamic conditions, while low-temperature synthesized NCO 150 and NCO 120 catalysts were found to form defect-rich non-stoichiometric complexes with respective Co/Ni stoichiometries of 1.39 and 1.55.

While knowing the identified defect sites could act as the catalyst centres promoting oxygen kinetics as previous literature suggests,[39] the main objective of the current study is to understand the effect of alteration in the stoichiometry on the catalytic activity and the battery performance. Following the concepts in molecular orbital theory, a strong interaction between the atomic orbitals of the catalyst site and the atomic orbitals of the reduced oxygen intermediates is needed to have strong adsorption of the intermediate reduced oxygen compounds ($Li_{2-x}O_2$) to the surface, facilitating a highly efficient Li–O_2 battery operation.[40] According to crystal field theory, as the transition metals coordinate with anionic groups such as oxides, the d-band splits into two energy levels, where the low energy threefold (d_{xy}, d_{yz}, and d_{xz}) t_{2g} orbitals are called the bonding orbitals, and the other two degenerate orbitals at a higher energy level (e_g base) are called the anti-bonding orbitals. According to Lund's rule and the Aufbau principle, electrons start to fill
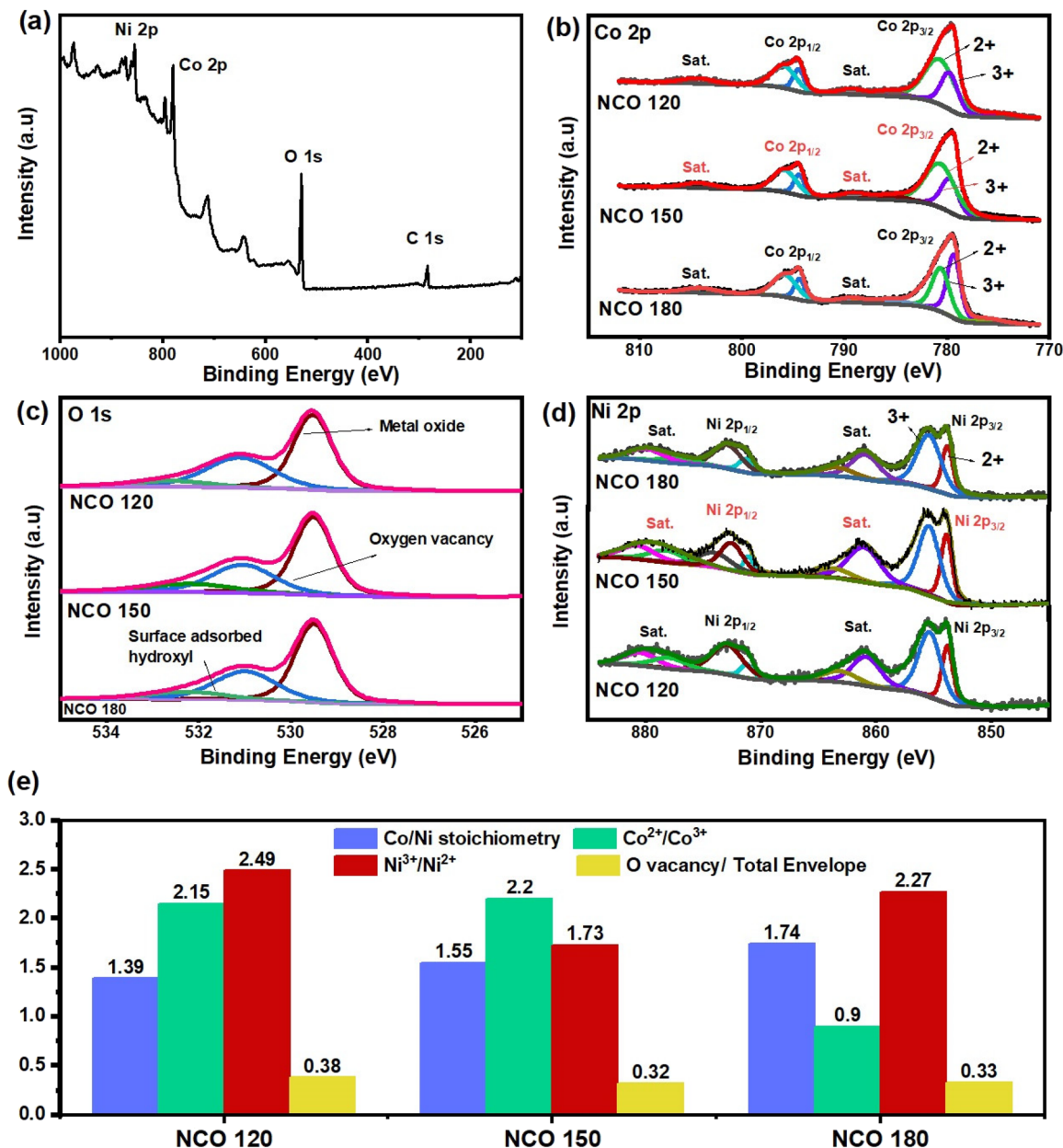
Fig. 3 XPS analysis: (a) survey spectrum, (b) Co 2p spectra, (c) O 1s spectra, (d) Ni 2p spectra of as-synthesized $NiCo_2O_4$ catalysts on Ni foam, and (e) extrapolated co-relations *via* peak area analysis.

from the t_{2g} orbitals, and if only the bonding orbitals are filled in the catalyst site, the reduced oxygen intermediates can bond at the vacant e_g anti-bonding orbitals, making it challenging to acquire strong adsorption in scenarios where the e_g orbitals are highly occupied. Accordingly, a high catalytic activity can be expected for Ni^{3+} ($t_{2g}^6 e_g^1$) with its unsaturated e_g orbital occupation, compared to highly e_g orbital filled Ni^{2+} ($t_{2g}^6 e_g^2$) and Co^{2+} ($t_{2g}^5 e_g^2$) ions. Amongst the three derived Ni–Co oxides, NCO 120 presents the highest Ni^{3+}/Ni^{2+} ratio (2.49) based on the deconvoluted peak area, compared to the ratios of 1.73 and 2.27 for NCO 150 and NCO 180 spinel structures, respectively. Hence, a high cata-

lytic activity can be expected from the engineered NCO 120 structure with favourable e_g occupation.

Electrocatalytic activity in aqueous medium

Before constructing Li–air battery cells, the OER and ORR catalytic activities of the synthesized NCOs were evaluated using a three-electrode configuration with a 1 M KOH aqueous electrolyte. Fig. S7(a and b)† present the LSV polarisation curves and the associated Tafel slopes, respectively. NCO 120 possesses the lowest onset potential of 1.56 V *vs.* RHE at 10 mA cm^{-2} current density and the smallest Tafel slope of 71 mV dec^{-1}, presenting a superior oxygen evolution activity over the other

two synthesized catalysts, NCO 150 and NCO 180. In addition to the faster kinetics, the NCO 120 catalyst exhibits long-term stability, as can be concluded from the galvanostatic chronopotentiometry in Fig. S8.† The stability of the catalyst over 50 hours of exposure to O_2 and to protonated reduced oxygen species such as OH^-, $OH^\bullet$ and $OOH^\bullet$ verifies the stability of the catalyst against possible parasitic reactions that could occur in aprotic Li–air batteries. Following the OER assessments, the catalytic activity towards ORR kinetics was also studied for all three synthesized materials. As indicated in Fig. S9,† all three materials draw higher reduction currents under an O_2-saturated environment, and the NCO 120 catalyst showed better activity with higher ORR current densities and peaks presenting at relatively higher potentials. The LSV curves are presented in Fig. S8(c).† Again, NCO 120 exhibits the best performance with the highest onset potential of 0.94 V vs. RHE, the highest halfwave potential of 0.88 V, and the highest current density of 0.47 mA cm^{-2} at 0.9 V, outperforming the other two NCO catalysts. Further assessment of ORR performances can be found in the ESI.†

The conducted experiments reveal the high amount of Ni^{3+} present in the electrode surface could significantly enhance the water electrolysis process, where both OER and ORR efficiencies follow the same order as the Ni^{3+}/Ni^{2+} atomic ratios, with NCO 120 exhibiting the highest catalytic activity, followed by the NCO 180 and NCO 150 catalysts, respectively. The study further implied the significance of the conducted stoichiometric optimization in Ni–Co oxides, which could be used as a simple technique to derive high-performing electrocatalysts. Moreover, the high surface area and the binder-free, well-interconnected unique surface structure of NCO 120 may further enhance the oxygen kinetics by exposing more reactive sites.

Aprotic Li–air battery analysis

Following the impressive ORR and OER performances in an aqueous medium, aprotic Li–air batteries were assembled using NCO 120 as the binder-free cathode, Li metal foil as the anode, and 1 M LiTFSl in TEGDME as the electrolyte. LAB cells with NCO 180 and NCO 150 cathodes were also constructed for comparison. The cyclic voltammetric (CV) curves recorded for the LABs in the voltage window of 2.0–4.5 V at a 0.2 mV s^{-1} scan rate are presented in Fig. 4(a). A detailed assessment of the CV curves and the associated electrochemical reactions and relevant product characteristics can be found in the ESI.† In summary, the NCO 120 cathode demonstrates superior performance with more positive ORR peak positions, less positive OER peak positions, and higher current densities. As is explained in the ESI,† it is noteworthy that the stoichiometric changes engineering a favourable surface electronic structure with plentiful unsaturated e_g orbital coordinates could lead to the high adsorption in NCO 120, supporting the formation of well-adsorbed reaction intermediates, allowing an easy decomposition of the discharged products which are possibly weakly crystalline in nature. The ability to decompose a higher portion of Li_2O_2 at a lower overpotential could suppress the

amount of singlet oxygen ($^1O_2$) that could be generated during the decomposition of the discharged products at higher potentials, where singlet oxygen has been identified as the main culprit causing parasitic reactions during Li–O_2 battery cycling.[16]

The superior performance of the NCO 120 cathode is further investigated using the charge–discharge profiles of the LABs presented in Fig. 4(b). The discharge capacities of the batteries follow the order of NCO 120 > NCO 180 > NCO 150, following the same pattern observed with the aqueous medium. The initial discharge capacities of 5079 mA h g^{-1} and 8431 mA h g^{-1} showed by NCO 150 and NCO 180 based LABs, respectively, are only 36.9% and 61.3% of the specific discharge capacity of 13 759 mA h g^{-1} achieved by the NCO 120 cathode-based battery. In addition to the remarkable catalytic activity displayed by NCO 120 owing to the abundant presence of surface catalytic sites featuring unsaturated e_g orbitals as discovered through TEM and XPS studies, the high surface area and interconnected mesoporous microstructure, as evidenced by BET and SEM studies, can also be considered as the main contributors to its superior charge–discharge performance. This is particularly evident in its ability to accommodate a substantial quantity of nanosized Li_2O_2 crystals and amorphous discharge products. The lowest observed charge voltage plateau of 3.89 V and the highest discharge voltage plateau of 2.80 V, along with the minimal charging overpotential of 1.09 V, are distinctive features of the NCO 120-based LAB, confirming the high affinity of it towards the reaction intermediates. These characteristics further underscore its superior catalytic powers compared to the NCO 150 and NCO 180 microstructures, which exhibit significantly higher overpotentials of 1.46 V and 1.22 V, respectively, with limited activity towards OER and ORR.

The cyclability of NCO 120 and NC 180 cathode-based LABs was evaluated using the charging and discharging method at a current rate of 100 mA g^{-1} with a limited discharge capacity of 500 mA h g^{-1}. Fig. 4(c) and (d) present the resultant charge–discharge curves. The LAB constructed with NCO 120 demonstrated the longest cycle life, successfully working up to 173 continuous cycles. In contrast, the LAB with the NCO 180 cathode only lasted for 84 cycles. The long cyclability exhibited the stability of the catalyst over a prolonged period. The exhibited excellent cyclability of the NCO 120-based LAB also surpasses the performances of many other $NiCo_2O_4$ and related-spinel cathode-based Li–air and Li–O_2 batteries, as presented in Fig. 6(a).[41–45]

In addition to individual charge–discharge curves, the respective potentials at the end of each step were also recorded. As illustrated in Fig. 4(e), the charge potential remains mostly constant at around 3.85 V for the first 80 cycles before it starts to rise gradually. This observation validates the undiminished OER activity, and the availability of the catalyst sites to get attached to the reaction intermediates. The discharge potential, on the other hand, dropped steadily throughout the cyclic study until it reached the cut-off potential of 2.0 V during the 173rd cycle for NCO 120. In contrast,
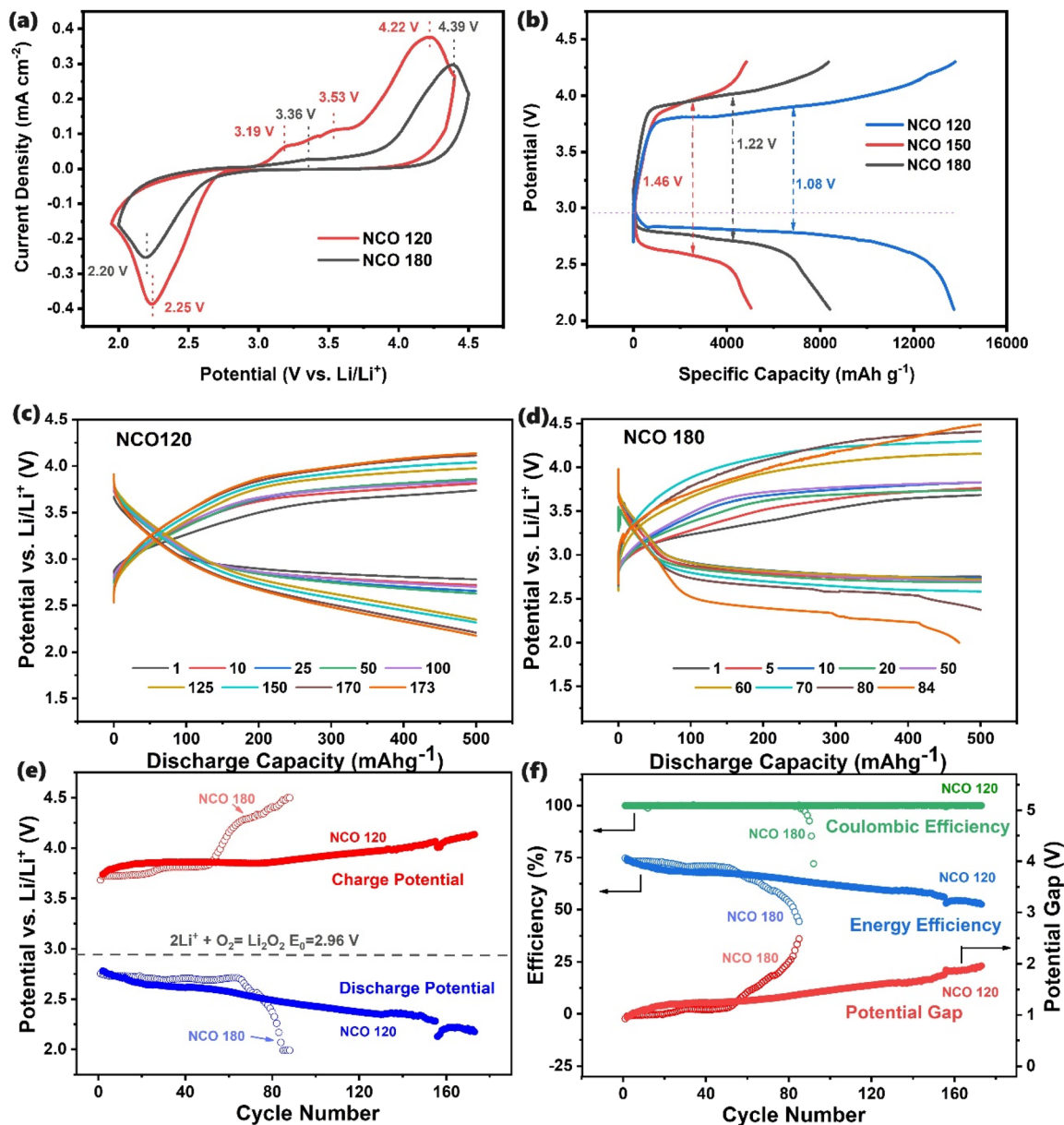
Fig. 4 (a) CV analysis @0.2 mV s⁻¹ and (b) full discharge–charge @100 mA g⁻¹, and selected discharge–charge curves of (c) NCO 120 and (d) NCO 180 cathode-based LABs operated at 100 mA g⁻¹ for a limited capacity of 500 mA h g⁻¹. (e and f) Cycle life and performance analysis of LABs with NCO 120 and NCO 180 based cathodes with cut-off discharge capacity of 500 mA h g⁻¹ with 1 M LiTFSl dissolved in TEGDME electrolyte.

the relatively stable charge and discharge potentials rose and dropped sharply, respectively, by the 50th cycle during the cyclability analysis of the NCO 180-based LAB, causing a sharp rise in the potential gap, as can be seen in Fig. 4(d) and (f). We believe that either the unfavourable physical properties of the NCO 180 cathode, where the attached 2D sheets could lose their contact with the surface of the cathode, or the fast-decaying catalytic properties are responsible for the reduced activity. Even though the NCO 180-based LAB performed marginally better in the first few cycles, the overall impressive, smooth, and steady operation was observed with the NCO 120-based

Li–air battery system during the cyclability analysis, performing 173 cycles in the dry air medium for a span of 3460 hours by maintaining a lower potential gap and full cyclability. Further detail on the characteristic behaviour can be found in the ESI.† The high oxygen, LiO_2, and Li_2O_2 adsorption capabilities of the NCO 120-based cathode attributed to its supportive surface electronic structure may contribute to long cyclability and low charge/discharge overpotential by providing high adsorption capacity for the reaction intermediates. Hence, a swift decomposition at lower charging overpotentials was achieved by forming a nano-crystalline layer of $Li_{2-x}O_2$

well-attached at the surface during discharge while suppressing the discharge product migration to the electrolyte and the formation of a large toroid of Li_2O_2.

We then studied the performance of the NCO 120 LAB at higher current ratings. In principle, lower discharge capacities were expected at higher current densities since the discharge product is expected to form a thin layer at the cathode surface, ruling out further discharge by quickly covering all available sites for oxygen adsorption. Further, the decrease in oxygen diffusion depth contributes inversely to achieving higher discharge capacities at higher current densities.[8] As the current density increased to 200 mA g^{-1}, the NCO 120 LAB showed an impressive discharge capacity of 10 030 mA h g^{-1} with a 93% coulombic efficiency, as indicated in Fig. 5(a). This achievement constitutes a noteworthy 72.7% of capacity retained compared to the discharge capacity obtained at a 100 mA g^{-1} current rating. The discharge capacity decreased to 4945 mA h g^{-1} as the current density was further raised to 400 mA g^{-1}. This change was accompanied by a coulombic efficiency of 84.6% and a charge/discharge overpotential of 2.19 V, underscoring the challenges in maintaining full reversibility after full discharge, thus indicating reduced capacity. The cyclability of the NCO 120 LAB was impressively high at 200 mA g^{-1} and 400 mA g^{-1} current densities, operating at nearly 100% coulombic efficiency for 96 and 59 cycles, respectively, as indicated in Fig. 5(b–d). In addition, the battery lasted for another 16 cycles of operation before its performance decayed to <50%

charge retention as the cells were cycled at a rate of 400 mA g^{-1}. Further, two voltage plateaus related to fast chraging can be found in the studies. These are more likely to be associated with the decomposition of the surface-grown nanocrystals of $Li_{2-x}O_2$ at a lower potential and the large toroid of Li_2O_2 needing a relatively high potential to get decomposed. The presence of the voltage plateaus in similar potential ranges as the peak positions observed during the cyclic voltammetry studies further justifies these observations. In addition, a smooth charging step under a 100 mA g^{-1} rate of charge is noticeable, and it suggests that the formation of a nanocrystalline/amorphous product of $Li_{2-x}O_2$ is favourable during the discharging step. It is noteworthy that the limiting factor for terminating the battery cycling occurred as the discharge process reached its cut-off condition, unlike the typical scenario of the inability to complete recharge in the effective potential window. Therefore, this could suggest that the catalyst is exhibiting far greater OER performance than ORR activity. Restricted oxygen diffusion with limited O_2 content in dry air and the changes in the cathode surface/electrolyte during continuous cycling may trigger the reduction in the discharge potential.

Fig. 6(a) presents a comparison between the NCO 120 electrode and other reported LAB cathodes in the literature. The figure demonstrates the stable and outperforming bifunctional catalytic activities of NCO 120. For instance, a slightly improved OER onset potential and ORR halfwave potential
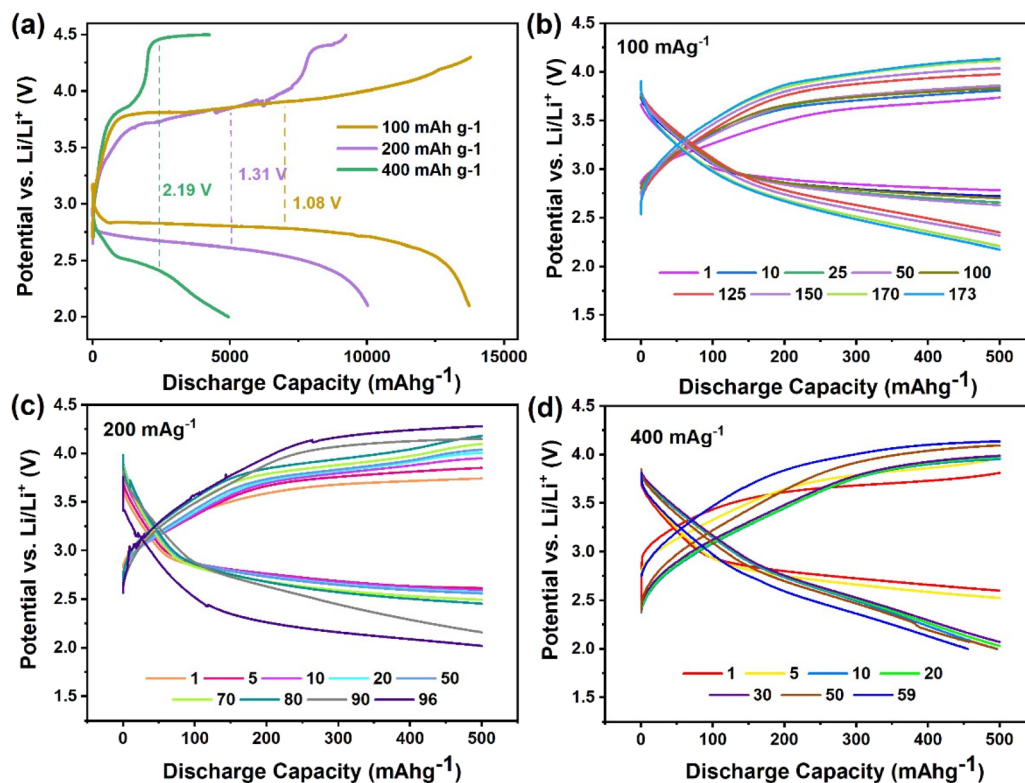

Fig. 5 Electrochemical performance analysis of NCO 120 cathode-based LABs under different current densities: (a) full discharge–charge capacity, selected discharge–charge curves under a current density of (b) 100 mA g^{-1}, (c) 200 mA g^{-1}, and (d) 400 mA g^{-1}.
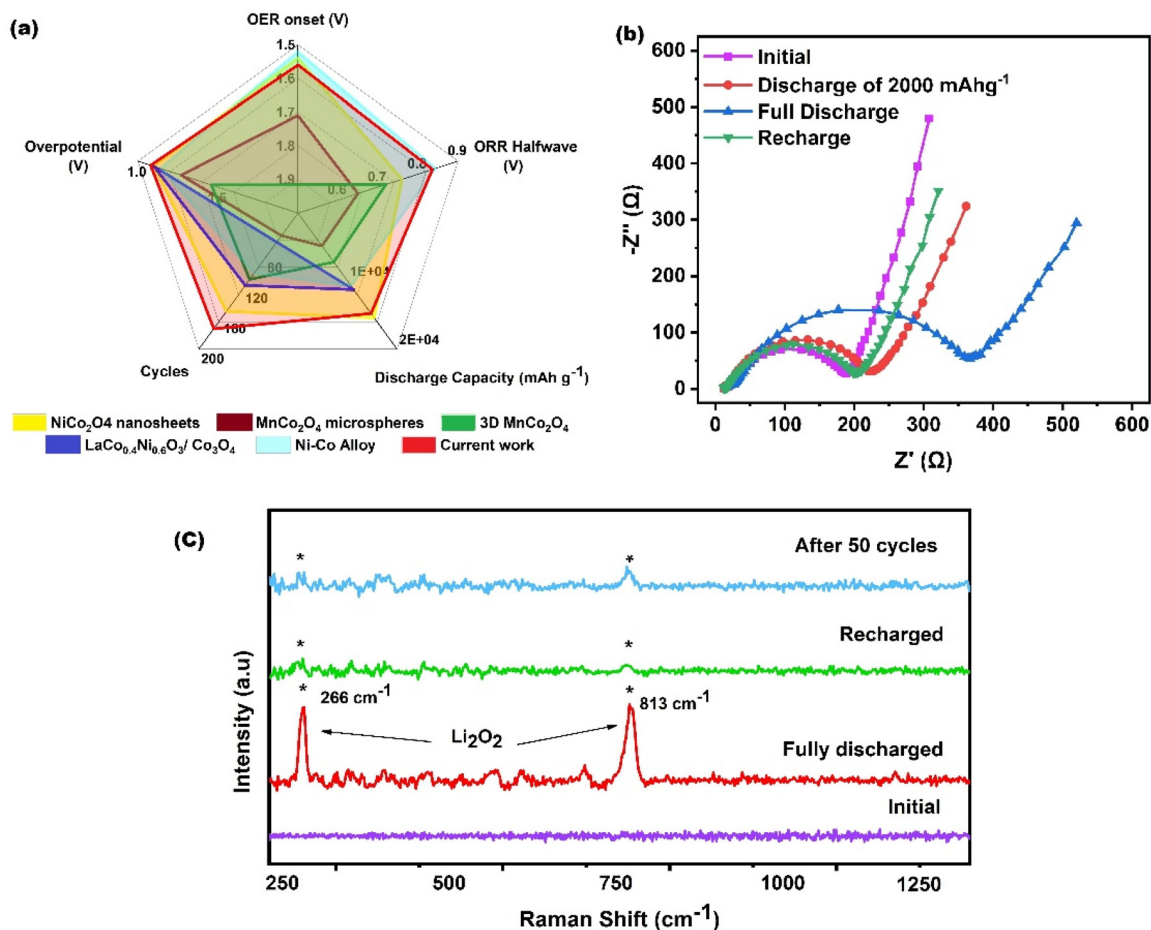
Fig. 6 (a) Literature comparison,[41–45] (b) EIS analysis, (c) *ex situ* Raman analysis of LAB cells with the freestanding NCO 120 cathode at various levels of discharge and charge.

were achieved by Chang *et al.*[45] with the aid of a hybridized carbonaceous structure, where their Co–Ni alloy was enclosed within N-doped graphene. However, this approach seems to have drawbacks. Specifically, it led to the system's deterioration, reducing the battery's lifespan, as it couldn't endure a significant number of charge/discharge cycles, possibly due to the electrochemical instability of the graphene at higher potentials. This prompted us to delve deeper into the associated reaction mechanism and gain further insights into the exceptional bifunctional catalytic activity of the freestanding NCO cathode. Consequently, we conducted *ex situ* analysis of the discharge and charge products using Electrochemical Impedance Spectroscopy (EIS), SEM, and Raman spectroscopy.

Since a bottom-up growth approach has been used to grow the NCO catalysts on the Ni foam substrate, a superior interfacial bonding with good ohmic contact between the catalyst sites and the substrate is expected. EIS analysis was conducted on LAB cells with the freestanding NCO 120 cathode at various levels of discharge, as presented in Fig. 6(b), with the battery discharged/charged at 100 mA h^{-1} current density, using a sinusoidal signal with the amplitude of 5 mV$_{pp}$ in the frequency domain of 0.01–1000 Hz. In the Randles circuit fitted

Nyquist plot obtained for the LABs, the high-frequency interception of the semicircle with the real axis is related to the series ohmic resistance (R_s), which is a sum of the lead resistance, contact resistance, and ionic resistance of the electrolyte and the separator, while the semicircle denotes the charge transfer resistance (R_{ct}) at low frequencies. The lowest R_s and R_{ct} with respective values of 11.8 Ω and 168.3 Ω were found initially before the discharge. The ohmic resistance increased to 12.6 Ω, and 16.3 Ω, respectively, after being discharged to 2000 mA h g^{-1} depth and discharged fully, before decreasing to 12.2 Ω after being charged back. The charge transfer resistance also followed the same trend, where the respective values of 196.5 Ω, 362.7 Ω, and 177.4 Ω were recorded after the phases of limited discharge (2000 mA h g^{-1}), full discharge, and recharge. Irrespective of the identified surface defects and favourable electronic structure, the overall insulating characteristics of metal-oxides may have contributed heavily to the initial resistance. An increase in the R_s and R_{ct} during the discharge is associated with the formation of the surface adsorbed Li$_2$O$_2$ insulating layer on the cathode, and the increased ionic resistance is also attributed to the Li-ion concentration reducing considerably while it participates in

forming non-soluble Li_2O_2. It is noteworthy to mention that the impedance increased only marginally after discharge to 2000 mA h g^{-1}, and more importantly, after the first charge, the R_s and R_{ct} reduced substantially, almost reaching the initial conditions, verifying the full decomposition of the discharged product, which further implies the excellent redox kinetics in the NCO 120 freestanding cathode-based LAB. Further, the identified remarkable recoverability of the cell after being charged back may be pivotal in demonstrating the excellent cycle performances of the NCO 120-based cells.

Raman analysis is a potent technique for analyzing the exiting phases of discharge products on the air electrode, and it could identify the presence of a range of electrochemically and chemically generated Li species, which affect the cyclability and efficiency of the LAB. The conducted *ex situ* Raman analysis on the battery cathode obtained at different stages of the discharge and charge is presented in Fig. 6(c). Apparently, the synthesized starting material is free of Li-related Raman peaks in the area of interest. Upon full discharge, two distinct peaks at 266 and 813 cm^{-1} arose, which could be assigned to the desired discharge product of Li_2O_2.[46] Almost full reversibility of the battery is demonstrated as the peaks disappear upon charging, where only a slight trace can be identified. Further, the Raman spectrum obtained for the NCO 120 cathode after 50 cycles indicates residual Li_2O_2 left at the cathode surface. This explains the loss of capacity as more undecomposed discharge products accumulate at the cathode surface as the cycle number progresses. In addition to reversibility, the results further verify that none of the parasitic products, like Li_2CO_3 or LiOH, were formed in the system in detectable quantities. High contributions from the freestanding cathode architecture and the high OER activity of the NCO 120 catalyst may pave the path towards a longer life span by minimizing the early degradation of the cathode materials and electrolytes. The detection of strong peaks and the respective peak positioning further indicate the formation of amorphous layers of Li_2O_2 over crystalline toroidal-shaped particles since amorphous Li_2O_2 is easily detectable at relatively higher frequencies[42] (compared to crystalline Li_2O_2) due to its marginally uncoordinated defective nature and shorter O–O bond length.

The conducted *ex situ* SEM analysis of the NCO 120 cathode material at various stages of the discharge–charge process also provides further insight into the discharge mechanism, as presented in Fig. S10.† It was evident that the discharged product fully covered the cathode surface as the battery was fully discharged, as indicated in Fig. S10(b and e),† compared to the cathode before discharge as in Fig. S10(a and c).† The reversibility of the process is proven as the formed Li_2O_2 was decomposed upon charging, leaving the morphological features of the charged cathode (Fig. S9(c and f)†) very similar to those of the initial NCO 120 cathode as indicated in Fig. S9(a and c).† Further, it is noteworthy that the discharged product was deposited over the surface of the cathode as an amorphous coating without any crystalline shape, well distributed along the cathode surface. The observations made here validate the previous observations made during the cyclic voltammetry, gal-

vanostatic charge–discharge, and Raman microscopic analysis, which favour the growth of nanocrystalline/amorphous discharge products over the growth of toroidal-shaped crystals of Li_2O_2, especially at the current rate of 100 mA g^{-1}. High abundance of catalytic sites throughout the cathode surface and the identified superior catalytic activity of the stoichiometrically modified Ni–Co oxide catalyst material with the vacant d-orbital sites with easy accessibility for the charge/discharge intermediates are expected to be favouring the growth of easily decomposable surface-attached discharge products, promoting superior LAB performance.

Considering the observations made *via* EIS, *ex situ* Raman, and *ex situ* SEM studies, the mechanism presented in Fig. S11† seems to be well suited for describing the discharging–charging process of the studied NCO 120 cathode-based LABs. As the battery discharged, a thin layer of discharge product gradually covered the voids in the surface of the cathode, and this layer largely dissipated as the battery underwent recharging. Despite earlier conjectures about the passivation of Li–air battery cathodes due to the formation of a thin layer of discharge product on the surface, limiting the discharge capacity, our current study challenges this notion. We achieved a substantial discharge capacity while generating surface adsorbed LiO_2 and Li_2O_2. To attain such a substantial surface coating of the discharge product and to achieve long endurance during cycling, we postulate the following,

1. The defect-rich cathode facets have a supportive electronic structure, promoting fast adsorption of reaction intermediates, which encourages discharge products to stay intact on the cathode surface even though a solvent with a high donor number (DN) was used. The reaction mechanism for the electrochemical reduction of O_2 occurring at the air–electrolyte–catalyst three-phase interface is presented in reaction 1.

$$Li^+_{(s)} + O_{2(g)} + e \rightarrow LiO_{2(ads)} \tag{1}$$

In reaction 1, the formed superoxide radical ($O_2\cdot^-$) reacts with Li^+ forming LiO_2. Since the produced lithium superoxide stayed in contact with the electrode surface, it could be assumed that the final discharged product of Li_2O_2 was mostly produced by the second electron transfer (as previously introduced) over the disproportionation of LiO_2.

$$Li^+_{(s)} + LiO_{2(ads)} + e \rightarrow Li_2O_{2(ads)} \tag{2}$$
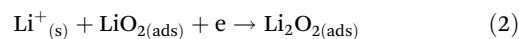
2. The coated discharged product is amorphous and is permeable to Li^+ diffusion, allowing further discharge.

3. The catalyst exhibits high OER activity owing to the presence of unsaturated e_g orbital coordination sites, and the Li_2O_2 is relatively conductive and easily decomposable, enabling a stable LAB operation over 170 cycles with a low charging overpotential.

4. Since the side products, such as Li_2CO_3, were not detected during the study in substantial quantities, it could be assumed that the reversible operation of the LAB cells took place without many obstacles related to parasitic reactions due to the following.

a. As the reduced reactive oxygen species, LiO_2, and Li_2O_2, mostly stayed in contact with the surface of the catalysts, it could be assumed that the electrolyte was less exposed to parasitic reactions during the discharging involving possible nucleophilic substitutions and H atom abstractions by the mentioned species.

b. Since Li_2O_2 stayed intact on the electrode surface as an amorphous coating and since it was quickly decomposed upon charging, it could suppress the extensive singlet oxygen generation, protecting the electrolyte from prolonged exposure.

c. The freestanding NCO 120 cathode remained resistant to parasitic reactions, unlike carbon-based electrodes, which were reported to be susceptible.

d. The presence of a small CO_2 quantity ($\sim 0.04\%$) in dry air does not seriously affect the reversibility of the LAB cells, and the number of parasitic reactions that could occur in the air medium *via* generating highly reactive protonated reduced oxygen species as HOO*, HOO^-, and HO* was substantially reduced as the main proton source (moisture) was removed from the medium.

Only providing limited details on the surface facets and their adsorption energies could be found as a limitation of the study, and they could have a significant correlation with the battery performance, which is worth investing in the future. Even though we used Ni–Co oxides to demonstrate the effect of stoichiometry on catalytic performance, the concept could be expanded to other systems with greater effectiveness in the future. Since a more sensible pathway towards achieving a true Li–air battery involves using a solid-electrolyte, separating the Li metallic anode from the environment, it is particularly important to understand the effectiveness of derived solid electrocatalysts with solid electrolytes and the associated electrochemistry, where the solution-based redox mediators cannot be expected to be compatible.

reported with spinel oxides, indicating the significance of the study. Even though the study used the spinel structures of Ni–Co oxides, the discussed strategy could be extended for optimizing the stoichiometric ratios in other similar structures of oxides, sulfides, phosphides, *etc*. The introduced highly efficient cathode catalytic system could be coupled with a solid electrolyte to develop long-term durable Li–air battery systems in future research by protecting the battery anode against contaminants.

Author contributions

Shadeepa Karunarathne: conceptualization, methodology, investigation, formal analysis, visualization, writing – original draft. Yasun Y. Kannangara: investigation, visualization. Chirag R. Ratwani: investigation, visualization, writing – review & editing. Chanaka Sandaruwan: investigation, visualization. W. P. S. L. Wijesinghe: investigation, visualization. Ali Reza Kamali: resources, supervision, funding acquisition, conceptualization, writing – review & editing. Amr M. Abdelkader: resources, supervision, funding acquisition, conceptualization, writing – review & editing.

Conflicts of interest

The authors declare no conflict of interest.

Acknowledgements

Conclusion

In summary, we developed a series of Ni and Co binary oxides with unique hierarchical 3D structures by controlling nucleation and growth during hydrothermal processes. The stoichiometry, electronic properties, morphology, and distortions in the crystal structure of the derived structures were found to depend on the parameters of the synthesis process, yielding three distinctive structures. The material analysis suggested that the NCO 120 has the most favourable catalytic structure with plentiful unsaturated e_g orbital coordinates formed through substitutional disorder and a well-formed hierarchical network. This electrode demonstrated exceptional performance, achieving a discharge capacity of $13\,759$ mA h g^{-1} at a current density of 100 mA g^{-1}. Moreover, the cell operated continuously for 3460 hours, completing 173 charge/discharge cycles while maintaining a capacity of over 98% coulombic efficiency in a dry-air environment. This performance surpasses the performances of the constructed LABs with NCO 150 and NCO 180, and the performances of many other LABs

References

1 J. F. Mercure, P. Salas, P. Vercoulen, G. Semieniuk, A. Lam, H. Pollitt, P. B. Holden, N. Vakilifard, U. Chewpreecha, N. R. Edwards and J. E. Vinuales, *Nat. Energy*, 2021, **6**(12), 1133–1143.

2 L. Kong, Z. Li, W. Zhu, C. R. Ratwani, N. Fernando, S. Karunarathne, A. M. Abdelkader, A. R. Kamali and Z. Shi, *J. Colloid Interface Sci.*, 2023, **640**, 1080–1088.

3 M. Salado and E. Lizundia, *Mater. Today Energy*, 2022, **28**, 101064.

4 Z. Luo, C. Ji, L. Yin, G. Zhu, B. B. Xu, Y. Wang, T. X. Liu, X. Zhuge and K. Luo, *Mater. Today Energy*, 2020, **18**, 100559.

5 L. N. Song, W. Zhang, Y. Wang, X. Ge, L. C. Zou, H. F. Wang, X. X. Wang, Q. C. Liu, F. Li and J. J. Xu, *Nat. Commun.*, 2020, **11**(1), 1–11.

6 N. Imanishi and O. Yamamoto, *Mater. Today Energy*, 2019, **4**, 100031.

7 G. A. Attard, P. G. Bruce, E. J. Calvo, Y. Chen, L. A. Curtiss, D. Dewar, J. H. J. Ellison, J. Fernández-Vidal, S. A. Freunberger, X. Gao, C. P. Grey, L. J. Hardwick, G. Horwitz, J. Janek, L. R. Johnson, E. Jónsson, S. Karunarathne, S. Matsuda, S. Menkin, S. Mondal, S. Nakanishi, N. Ortiz-Vitoriano, Z. Peng, J. P. Rivera, I. Temprano, K. Uosaki, E. D. Wachsman, Y. Wu and S. Ye, *Faraday Discuss.*, 2024, **248**, 210–249.

8 S. Hyun, B. Son, H. Kim, J. Sanetuntikul and S. Shanmugam, *Appl. Catal., B*, 2020, **263**, 118283.

9 I. V. Zenyuk, P. K. Das and A. Z. Weber, *J. Electrochem. Soc.*, 2016, **163**, F691.

10 C. R. Ratwani, S. Karunarathne, A. R. Kamali and A. M. Abdelkader, *ACS Appl. Mater. Interfaces*, 2024, **16**(5), 5847–5856.

11 Editorial, *Nat. Catal.*, 2019, **2**(9), 735–735.

12 J. H. Kim, A. G. Kannan, H. S. Woo, D. G. Jin, W. Kim, K. Ryu and D. W. Kim, *J. Mater. Chem. A*, 2015, **3**, 18456–18465.

13 C. K. Lee and Y. J. Park, *Nanoscale Res. Lett.*, 2015, **10**, 319.

14 P. Sennu, M. Christy, V. Aravindan, Y. G. Lee, K. S. Nahm and Y. S. Lee, *Chem. Mater.*, 2015, **27**(16), 5726–5735.

15 B. M. Gallant, R. R. Mitchell, D. G. Kwabi, J. Zhou, L. Zuin, C. V. Thompson and Y. Shao-Horn, *J. Phys. Chem. C*, 2012, **116**, 20800–20805.

16 N. Mahne, B. Schafzahl, C. Leypold, M. Leypold, S. Grumm, A. Leitgeb, G. A. Strohmeier, M. Wilkening, O. Fontaine, D. Kramer, C. Slugovc, S. M. Borisov and S. A. Freunberger, *Nat. Energy*, 2017, **2**, 17036.

17 H. Osgood, S. V. Devaguptapu, H. Xu, J. Cho and G. Wu, *Nano Today*, 2016, **11**, 601–625.

18 T. Şener, E. Kayhan, M. Sevim and Ö. Metin, *J. Power Sources*, 2015, **288**, 36–41.

19 H. Hu, Y. Meng, Y. Mei, P. X. Hou, C. Liu, H. M. Cheng, M. Shao and J. C. Li, *Energy Storage Mater.*, 2023, **54**, 517–523.

20 P. Moni, S. Hyun, A. Vignesh and S. Shanmugam, *Chem. Commun.*, 2017, **53**, 7836–7839.

21 J. Wang, R. Zhan, Y. Fu, H. Y. Yu, C. Jiang, T. H. Zhang, C. Zhang, J. Yao, J. F. Li, X. Li, J. H. Tian and R. Yang, *Mater. Today Energy*, 2017, **5**, 214–221.

22 C. V. Amanchukwu, J. R. Harding, Y. Shao-Horn and P. T. Hammond, *Chem. Mater.*, 2015, **27**, 550–561.

23 J. Yuan, Z. Liu, Y. Wen, H. Hu, Y. Zhu and V. Thangadurai, *Ionics*, 2019, **25**, 1669–1677.

24 B. Sun, P. Munroe and G. Wang, *Sci. Rep.*, 2013, **3**(1), 1–7.

25 L. Ren, R. Zheng, D. Du, Y. Yan, M. He, Z. Ran, M. Li and C. Shu, *Chem. Eng. J.*, 2022, **430**, 132977.

26 N. C. Lai, G. Cong, Z. Liang and Y. C. Lu, *Joule*, 2018, **2**, 1511–1521.

27 Z. Zhou, L. Zhao, J. Wang, Y. Zhang, Y. Li, S. Shoukat, X. Han, Y. Long and Y. Liu, *Small*, 2023, **19**, 2302598.

28 X. Shi, S. L. Bernasek and A. Selloni, *J. Phys. Chem. C*, 2017, **121**, 3929–3937.

29 K. Bakken, O. G. Grendal and M. A. Einarsrud, *J. Sol-Gel Sci. Technol.*, 2023, **105**, 596–605.

30 G. E. Park, H. T. T. Le, H. S. Kim, P. N. Didwal and C. J. Park, *Ceram. Int.*, 2020, **12**, 46.

31 L. Cai, Y. Li, X. Xiao and Y. Wang, *Ionics*, 2017, **23**, 2457–2463.

32 Z. Yan, D. A. Keller, K. J. Rietwyk, H.-N. Barad, K. Majhi, A. Ginsburg, A. Y. Anderson and A. Zaban, *Energy Technol.*, 2016, **4**, 809–815.

33 T.-C. Chang, Y.-T. Lu, C.-H. Lee, J. K. Gupta, L. J. Hardwick, C.-C. Hu and H.-Y. T. Chen, *ACS Omega*, 2021, **6**, 9692–9699.

34 S. V. Devaguptapu, S. Hwang, S. Karakalos, S. Zhao, S. Gupta, D. Su, H. Xu and G. Wu, *ACS Appl. Mater. Interfaces*, 2017, **9**, 44567–44578.

35 M. Sun, S. Guo, Z. Wang, L. Zou, B. Chi, J. Pu and J. Li, *Electrochim. Acta*, 2020, **363**, 137235.

36 T. H. Ko, K. Devarayan, M. K. Seo, H. Y. Kim and B. S. Kim, *Sci. Rep.*, 2016, **6**(1), 1–9.

37 W. Zhang, H. Shen, M. Yin, L. Lu, B. Xu and D. Li, *ACS Omega*, 2022, **7**(19), 16494–16501.

38 Y. Y. Kannangara, S. Karunarathne, W. P. S. L. Wijesinghe, C. Sandaruwan, C. R. Ratwani, A. R. Kamali and A. M. Abdelkader, *J. Energy Storage*, 2024, **84**, 110717.

39 K. L. Bao, J. Y. Xu, N. F. Yu, J. B. Kuang, Z. T. Yang, H. Chen, J. L. Ye and Y. P. Wu, *Energy Fuels*, 2022, **36**, 6542–6551.

40 C. C. Li, W. Zhang, H. Ang, H. Yu, B. Y. Xia, X. Wang, Y. H. Yang, Y. Zhao, H. H. Hng and Q. Yan, *J. Mater. Chem. A*, 2014, **2**, 10676–10681.

41 X. Guo, J. Zhang, Y. Zhao, B. Sun, H. Liu and G. Wang, *ACS Appl Energy Mater*, 2019, **2**, 4215–4223.

42 S. Ma, L. Sun, L. Cong, X. Gao, C. Yao, X. Guo, L. Tai, P. Mei, Y. Zeng, H. Xie and R. Wang, *J. Phys. Chem. C*, 2013, **117**, 25890–25897.

43 Z. Li, Y. Lv, Y. Yu, J. Yin, K. Song, B. Yang, L. Yuan and X. Hu, *J. Alloys Compd.*, 2020, **817**, 152736.

44 M. Sun, S. Guo, Z. Wang, L. Zou, B. Chi, J. Pu and J. Li, *Electrochim. Acta*, 2020, **363**, 137235.

45 Z. Chang, F. Yu, Z. Liu, S. Peng, M. Guan, X. Shen, S. Zhao, N. Liu, Y. Wu and Y. Chen, *ACS Appl. Mater. Interfaces*, 2020, **12**, 4366–4372.

46 F. S. Gittleson, K. P. C. Yao, D. G. Kwabi, S. Y. Sayed, W.-H. Ryu, Y. Shao-Horn and A. D. Taylor, *ChemElectroChem*, 2015, **2**, 1446.